Check for updates

Angewandte Chemie International Edition

Angewandte International Edition Chemie GDCh German Chemical Society

How to cite: *Angew. Chem. Int. Ed.* **2026**, 65, e2469199
doi.org/10.1002/anie.2469199

RESEARCH ARTICLE OPEN ACCESS

Accelerated Discovery-to-Unveiling of High-Performance and Affordable Ammonia Electrode Process by Human–Machine Collaboration Framework

Yingying Cheng | Masaki Takeguchi | Abraham Castro Garcia | Ken Sakaushi

Research Center for Energy and Environmental Materials, National Institute for Materials Science, Tsukuba, Ibaraki, Japan

Correspondence: Ken Sakaushi (SAKAUSHI.Ken@nims.go.jp)

Received: 21 December 2025 | **Revised:** 17 April 2026 | **Accepted:** 23 April 2026

Keywords: dimensionally reduced reaction descriptors | electrochemical nitrate reduction reaction | human–machine collaboration | in-situ spectroscopy | kinetic model analysis

ABSTRACT

The electrochemical nitrate reduction reaction (eNO_3RR) to ammonia (NH_3) is a key for producing fuels during interstellar travel and an alternative to Haber–Bosch process. However, the complicated multi-electron/proton transfer electrode process of eNO_3RR makes affordable electrocatalyst discovery and its mechanistic understanding challenging. Herein, we established a human–machine collaboration framework by employing dimensionally reduced reaction descriptors which enables an accelerated data-driven discovery-to-unveiling of unconventional and high-performance eNO_3RR electrocatalysts with desirable element choice. Using the current density difference between nitrite (NO_2^-) reduction and hydrogen evolution as a descriptor, the optimal FeCoNiCuGa electrocatalyst was identified in a drastically short timeframe. Even compared with Pt or Rh, the FeCoNiCuGa exhibits a higher NH_3 production rate of 9.8 mmol mg_{cat}^{-1} at −0.3 V versus a reversible hydrogen electrode. Furthermore, together with a mechanistic study using rotating ring-disk electrode combined with a new kinetic model, in situ infrared spectroscopy unveiled that the adsorbed NO_2^- ($*NO_2^-$) plays a crucial role in the efficient electrode process: a moderate $*NO_2^-$ binding accelerates NH_3 formation whereas a weak binding leads to unfavorable reactions. Our work demonstrates that a comprehensive human–machine collaboration approach enables an accelerated discovery-to-unveiling of promising electrode processes, providing a feasible way to promote game-changing electrochemical technologies.

1 | Introduction

Unveiling microscopic mechanisms of multi-electron/-proton transfer electrode processes (MEPTs) is one of the grand challenges in science [1–6]. Even for the well-known archetype MEPTs of the hydrogen evolution reaction (HER) at well-defined single-crystal electrodes, we still do not fully understand how electrons and protons are transferred at electrified solid–liquid interfaces, neither theoretically nor experimentally, nor in combination [7–13]. A lack of a precise view of MEPTs is a key bottleneck in electrocatalyst design, delaying the advancement of next-generation electrochemical technology. Thus, it is game-changing to develop a methodology to accelerate promising electrocatalyst design with on-demand elements and spontaneously lead to a better understanding of the microscopic electrode process. In this context, renewable electricity-driven electrochemical ammonia (green-NH_3) synthesis is a typical MEPT that faces the issues.

NH_3 is a vital chemical that is widely used as a fertilizer, a fuel, a feedstock for pharmaceuticals, and an energy carrier on Earth and, in the future on the Moon or Mars [14, 15]. Moreover, NH_3 remains a critical chemical during interstellar travels. As

---

such, global NH_3 demand is expected to exceed 650 Mt by 2050 [16]. Currently, NH_3 synthesis relies on the Haber–Bosch (H–B) process, which operates at high temperatures and generates extra CO_2 emissions [17, 18]. The green-NH_3 synthesis offers an alternative to the H–B process, attracting tremendous attention over the past decades because it is based on electrolysis, making it suitable for operation outside Earth or for deployment in the limited space of interstellar spacecraft. Although N_2 is the most abundant nitrogen source, the high N≡N triple bond dissociation energy (941 kJ mol^{-1}) [19–22] limits NH_3 productivity toward N_2 electrochemical reduction. Water-soluble nitrate (NO_3^-) possesses a low N═O double bond dissociation energy (204 kJ mol^{-1}) [20, 23, 24], enabling favorable reaction kinetics for sustainable NH_3 synthesis from the electrochemical NO_3^- reduction reaction (eNO_3RR).

The eNO_3RR to NH_3 is an 8-electrons/9-protons MEPT involving the formation of various intermediates and byproducts [20, 25]. During eNO_3RR, subtle variations in intermediate binding and undesired intermediate stabilization can drastically affect reaction barriers and divert the pathway toward side reactions. $^*NO_2^-$ is identified as a key intermediate in NH_3 production, but the specific role of $^*NO_2^-$ in regulating NH_3 yields remains insufficiently explored. In this study, we employed the rotating ring-disk electrode (RRDE) technique alongside effective kinetic modeling to elucidate the complex NO_3RR electrode process. RRDE is a double-working-electrode configuration [26] that has been widely employed to investigate MEPTs (for example, oxygen reduction reactions, ORR) [27–35]. In RRDE configuration, electrochemical redox reactions occur at the disk electrode while the ring electrode detects the intermediate or product diffusing from the disk. By controlling rotation rate (ω), the plots of disk to ring current ($N\frac{I_D}{I_R}$, N is the collection efficiency) versus $\omega^{-0.5}$ enables in-depth probing of eNO_3RR intermediates and overall pathways [27–35]. As a result, we successfully uncovered theoretical insights for the rational design of multicomponent metal-oxide electrocatalysts.

Multicomponent metal-oxides exhibit high specific surface areas, tunable electronic structures, and strong synergistic interactions among different metal centers, all of which are advantageous for promoting efficient MEPT pathways [36, 37]. However, such benefits come at the cost of an extremely large compositional space resulting from the random combinations of multiple elements, making traditional intuition-driven screening strategies prohibitively time-consuming and inefficient. This bottleneck underscores the urgency of developing high-throughput, knowledge-guided approaches to rapidly identify promising candidates. Artificial intelligence (AI) is a powerful and transformative platform for electrocatalyst discovery, accelerating screening of multicomponent electrocatalysts by combining domain expertise with AI descriptor construction and data-driven learning [38, 39]. However, applying AI directly to MEPTs is nontrivial due to their complex reaction networks. For example, a typical MEPT eNO_3RR involves over a dozen intermediates and produces various products (NH_3, N_2, NO_2^-, et al), which makes selectivity prediction particularly challenging. Therefore, accurately identifying highly selective MEPT electrocatalysts requires AI models equipped with meaningful descriptors that are tailored to the mechanistic complexity of MEPTs.

Herein, we successfully bridge the gap between AI platforms and MEPTs by developing a directed simplification of MEPTs, enabling accelerated discovery of target materials and faster understanding of microscopic mechanisms. In this concept, a Bayesian optimization (BO)-based human–machine collaboration framework (HMC) was employed, which effectively shortened the screening period for eNO_3RR electrocatalysts. Using a dimensionally reduced reaction descriptor to provide a directed simplification of MEPT, the optimal quinary electrocatalyst of Fe, Co, Ni, Cu, and Ga based oxide material (denoted FeCoNiCuGa) was identified after 10 "training-suggestion-experiment" loops (1% trials in 3003 candidates). The NH_3 production rate of 9.8 mmol mg_{cat}^{-1} is achieved at −0.3 V versus the reversible hydrogen potential (RHE). Mechanistic studies including RRDE and in situ electrochemical infrared analysis reveal that high NH_3 yields originate from the rapid $^*NO_2^-$ formation and conversion, providing guidance for the design of selective eNO_3RR electrocatalysts.

2 | Results and Discussion

2.1 | Descriptor Establishment

Given the complexity of MEPTs, establishing accurate descriptors requires a comprehensive analysis of the overall reaction scheme. The eNO_3RR to NH_3 is considered a consecutive MEPT, consisting of NO_3RR to NO_2^- and electrochemical nitrite reduction reaction (eNO_2RR) to NH_3, with HER as a side reaction. In our approach, 15 elements (Cu, Fe, Mn, Sn, Bi, In, Zn, Ag, Au, Co, Ni, Ga, Mo, Sb, and Zr) were selected to construct quinary electrocatalysts. According to previous studies, Cu is responsible for NO_2^- formation [40], Fe and Co contribute to NO_3^- activation [41–43], Sn, Bi, In, Zn, Ag, Au, Ni act as adsorbed H (*H) mediator [44, 45], Ga, Mo, Sb, Zr modulate the electronic structure [46]. The quinary electrocatalysts were synthesized using the reported protocols [38]. In our model, the molar ratio of elements in the quinary catalysts was fixed at 1:1:1:1:1. A total of 3003 candidate catalysts (5 elements from 15 elements) were generated using a combinatorial enumeration approach. In order to construct a chemical composition search space, only the elemental composition was considered as the variable (Figure 1a).

To construct a training dataset, 10 quinary electrocatalysts were randomly selected from the 15 elements, followed by eNO_3RR, eNO_2RR, and HER linear sweep voltammetry (LSV), and eNO_3RR controlled potential electrolyses (CPEs) at −0.3 V versus RHE. NO_3RR products were quantified using colorimetric methods [47, 48]. All electrocatalysts exhibit higher current responses toward NO_3RR and NO_2RR than toward HER (Figure S1). During the eNO_3RR, the measured total current density consists of two contributions: the reduction current originating from NO_3^- itself and the current associated with the HER. Therefore, we performed mathematical integration of the eNO_3RR and HER LSV curves and calculated their difference to quantify the net eNO_3RR current (denoted as $j_{NO_3RR} - j_{HER}$, Figure 1b), which serves as an indicator of the net eNO_3RR current, following the same principle for the eNO_2RR versus HER ($j_{NO_2RR} - j_{HER}$, Figure 1c). The $j_{NO_3RR} - j_{HER}$ and $j_{NO_2RR} - j_{HER}$ of the training electrocatalysts were calculated and plotted against NH_3 yields

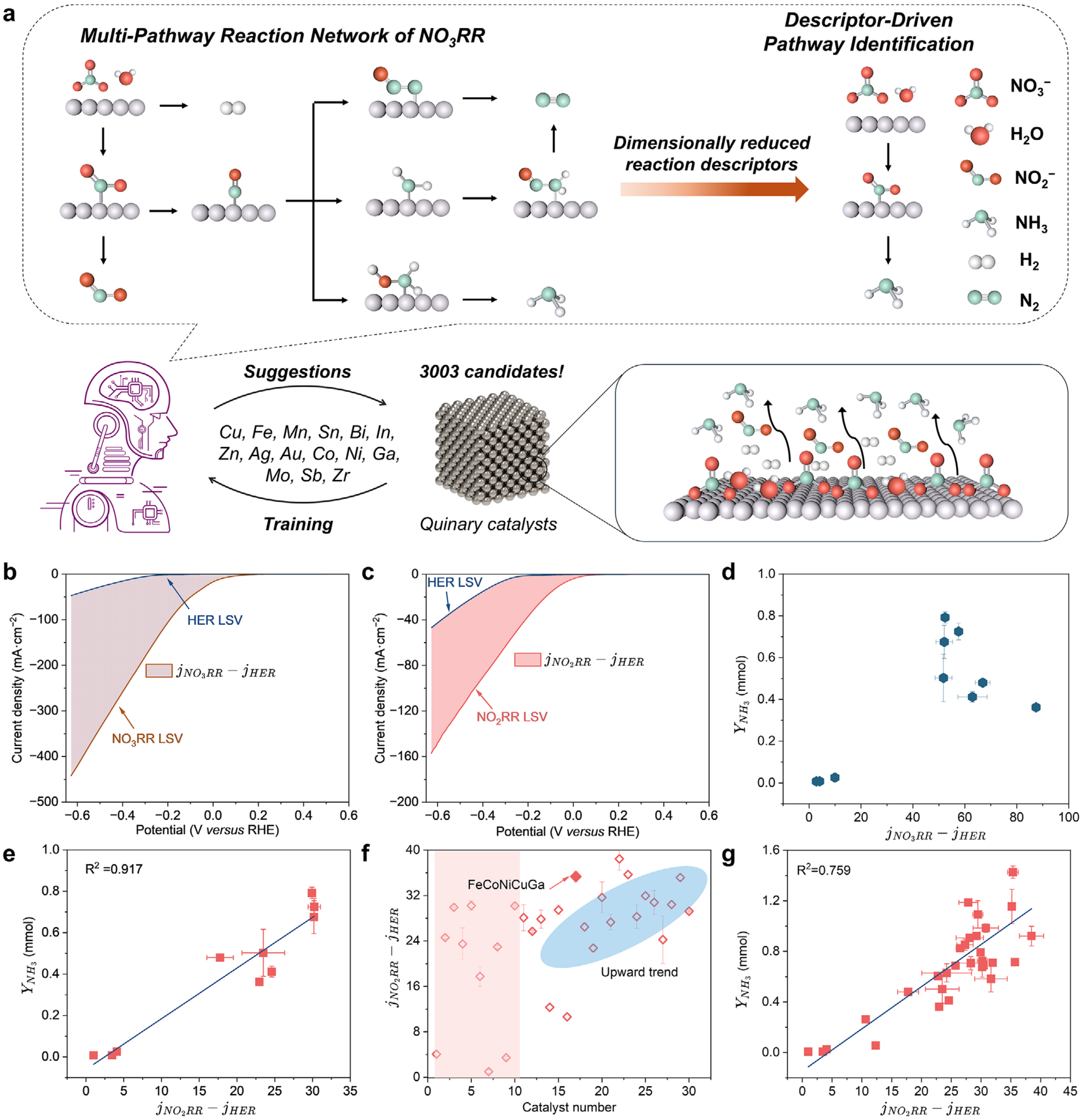

FIGURE 1 | (a) Schematic illustration of HMC applied to NO_3RR electrocatalyst screening. By employing dimensionally reduced reaction descriptors, the eNO_3RR-to-NH_3 pathway can be effectively extracted from the multi-pathway eNO_3RR reaction network. Schematic illustrations of (b) $j_{NO_3RR} - j_{HER}$ and (c) $j_{NO_2RR} - j_{HER}$ calculations from eNO_3RR, eNO_2RR, and HER LSV profiles. (d) Correlations of $j_{NO_3RR} - j_{HER}$ with Y_{NH_3} and (e) $j_{NO_2RR} - j_{HER}$ with Y_{NH_3} in the initial training dataset. (f) Plots of electrocatalyst number against $j_{NO_2RR} - j_{HER}$, and (g) plots of $j_{NO_2RR} - j_{HER}$ against Y_{NH_3} after 10 "training-suggestion-experiment" loops.

(Y_{NH_3}) from CPEs (Figure 1d,e). There is no clear correlation between $j_{NO_3RR} - j_{HER}$ and Y_{NH_3} (Figure 1d), but a strong linear correlation is observed between $j_{NO_2RR} - j_{HER}$ and Y_{NH_3} (R^2 value of 0.917) (Figure 1e), suggesting that $j_{NO_2RR} - j_{HER}$ is a reliable descriptor for the NO_3RR electrocatalyst.

The electrocatalyst compositions and $j_{NO_2RR} - j_{HER}$ were used as descriptors for HMC to predict promising electrocatalysts via a statistical model and optimization algorithms. In each loop, HMC gave two suggestions followed by the synthesis and electrochemical measurements of eNO_2RR, HER LSVs and eNO_3RR CPEs at −0.3 V. The newly obtained compositions and $j_{NO_2RR} - j_{HER}$ were incorporated into the dataset for the next loop and plotted against Y_{NH_3} to assess the correlation (Figure S2). After the first loop, the predicted electrocatalysts show a strong linear correlation between $j_{NO_2RR} - j_{HER}$ and Y_{NH_3}(R^2 value of 0.872) (Figure S2a), further confirming the high accuracy of the descriptors. At the fourth loop, the material consists of Fe, Co, Ni,

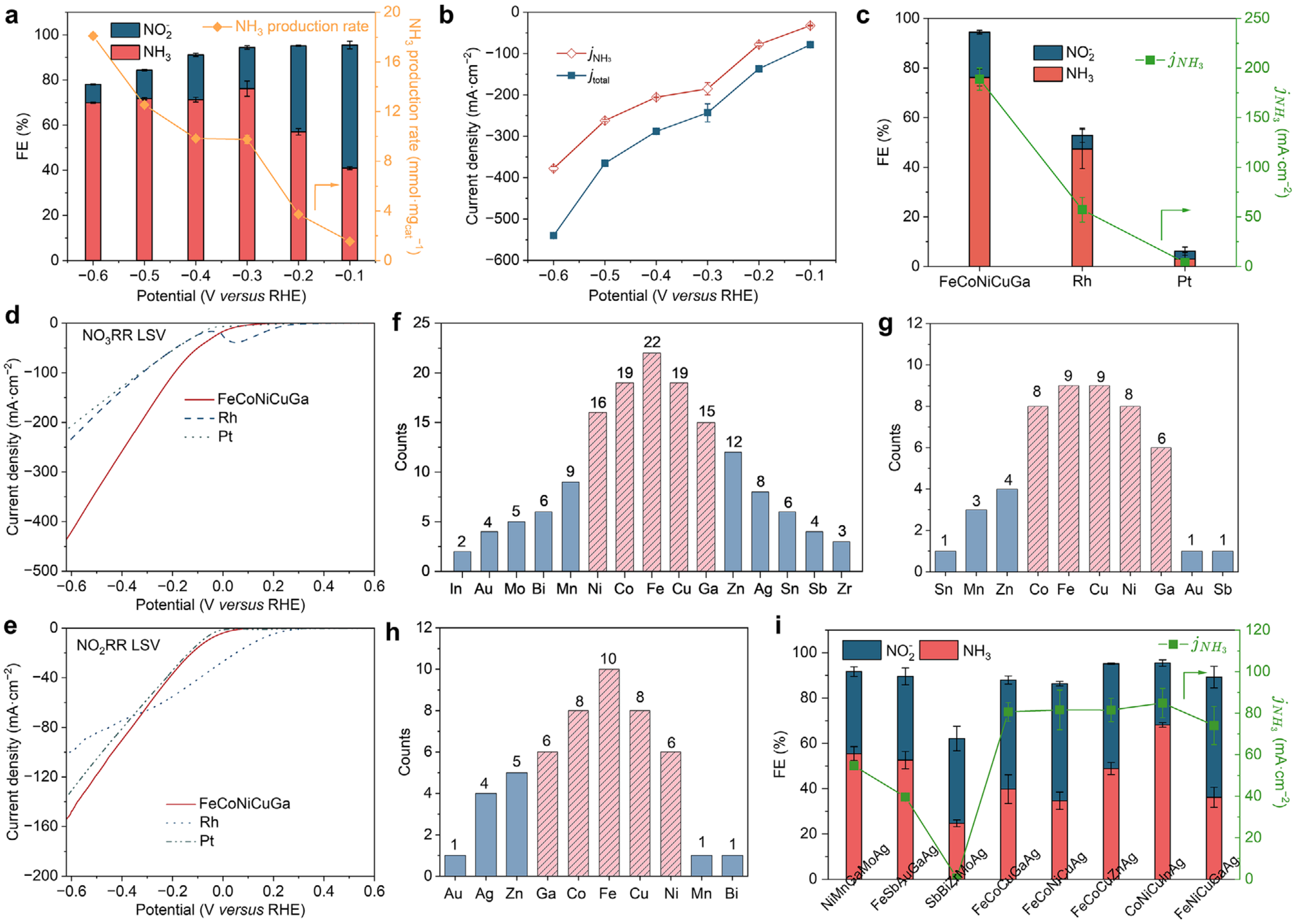

FIGURE 2 | (a) Products distribution and NH_3 production rates of FeCoNiCuGa during eNO_3RR CPEs in 0.1 M KOH + 1 M KNO_3. (b) The j_{total} and j_{NH_3} from eNO_3RR CPEs on FeCoNiCuGa. (c) Products distribution and j_{NH_3} of NO_3RR CPEs on FeCoNiCuGa, Pt, and Rh at −0.3 V. (d) NO_3RR and (e) NO_2RR LSV curves of FeCoNiCuGa, Pt, and Rh in 0.1 M KOH + 1 M KNO_3 and 0.1 M KOH + 0.2 M KNO_2. (f) Elemental occurrence frequencies across the full HMC dataset. Elemental occurrence frequencies in (g) the top 10 electrocatalysts ranked by Y_{NH_3}, and (h) the top 10 electrocatalysts ranked by $j_{NO_2RR} - j_{HER}$. (i) Products distribution and j_{NH_3} of NO_3RR CPEs on Ag-containing electrocatalysts at −0.3 V.

Cu, Ga (FeCoNiCuGa) has emerged as the optimal electrocatalyst with a highest Y_{NH_3} of 1.43 mmol. In subsequent loops, although $j_{NO_2RR} - j_{HER}$ exhibits an upward trend, the suggested electrocatalysts show lower NH_3 yields than FeCoNiCuGa (Figures 1f, S3). This performance saturation prompted the termination of the screening after 10 loops. In total, 30 electrocatalysts (10 from the initial training dataset and 20 suggested electrocatalysts) were synthesized, accounting for 1% of the 3003 candidates. A strong correlation between $j_{NO_2RR} - j_{HER}$ and Y_{NH_3} maintains after 10 loops (Figure 1g), confirming that HMC effectively accelerates the electrocatalyst screening and significantly reduces the experimental workload.

2.2 | Data-Driven and Mechanical Analysis

The eNO_3RR CPEs from −0.1 to −0.6 V versus RHE were conducted by using FeCoNiCuGa as the model system (Figure 2a,b). FeCoNiCuGa exhibits high NH_3 Faradaic efficiencies (FEs), total current densities (j_{total}) and NH_3 partial current densities (j_{NH_3}) over a wide potential range and the maximum NH_3 production rate of 18.1 mmol mg_{cat}^{-1} is achieved at −0.6 V (Figure 2a). At −0.3 V, the NH_3 production rate reaches at 9.8 mmol mg_{cat}^{-1}, outperforming platinum group metals (PGMs) such as Pt and Rh, showing its potential for large-scale implementation (Figure 2c). Rh has a high NO_2RR response (Figure 2e), but inferior eNO_3RR performance (Figure 2d) limits its NH_3 FE. HER was revealed to be the dominant reaction on Pt, suggesting its inferior performance as a NO_3RR electrocatalyst (Figure S4). A 12-hour CPE was conducted at −0.3 V to evaluate the durability of the FeCoNiCuGa (Figure S5). The current density remained almost constant throughout continuous operation and the NH_3 FE showed minimal variation over time, indicating stable electrocatalytic activity and selectivity of FeCoNiCuGa. The absence of any significant performance decay suggests that no functional degradation occurred. To determine electrocatalyst compositions, the structural analyses including x-ray diffractometry (XRD), scanning transmission electron microscopy (STEM), and x-ray photoelectron spectroscopy (XPS) of FeCoNiCuGa were performed (Figures S6–S8). An obvious electrocatalyst layer can be observed in the cross-sectional high-angle annular dark field (HAADF) STEM image of FeCoNiCuGa (Figure S7a). The EDS mapping of O, Fe, Co, Ni, Cu, and Ga elements show the uniform distribution, further confirming the even composition of FeCoNiCuGa (Figures S7b–g). The XPS analysis reveals that Fe, Co, Ni, and Cu exist as the mixed valence states, while Ga exists as the Ga(III) state in FeCoNiCuGa (Figure S8). FeCoNiCuGa displays in an amorphous matrix, where the synergistic interaction among the elements has a coordination effect in NH_3 formation.

To identify the high electrochemical properties of FeCoNiCuGa, we studied the correlations between the electrocatalyst composition and both the $j_{NO_2RR} - j_{HER}$ and Y_{NH_3}. The elemental occurrence frequencies of the total HMC dataset were counted first. Within this dataset, the Fe, Co, Cu, Ni, and Ga elements appear 22, 19, 19, 16, and 15 times, respectively, ranking the top five elements (Figure 2f). Analyses of the top 10 electrocatalysts ranked by Y_{NH_3} and $j_{NO_2RR} - j_{HER}$ show that Fe, Cu, Ni, Co, and Ga consistently appear with frequencies of 9, 9, 8, 8, and 6, and 10, 8, 8, 6, and 6, respectively (Figure 2g,h), showing the importance in NH_3 production. Notably, Ag appears four times in the top 10 $j_{NO_2RR} - j_{HER}$ but demonstrates no association with the high Y_{NH_3} (Figure 2g,h, Table S1). Excluding Ag-containing electrocatalysts from the HMC dataset improves the linear correlation between $j_{NO_2RR} - j_{HER}$ and Y_{NH_3} (R^2 value of 0.774) (Figure S9). The NO_3RR LSVs of Ag-containing electrocatalysts show onset potentials around 0.2 V (Figure S10) and high NO_2^- FEs upon CPEs at −0.3 V (Figure 2i), suggesting that Ag promotes eNO_3RR to NO_2^-. These results indicate that, despite Ag-containing electrocatalysts having high eNO_2RR activities, the NO_2^- accumulation ultimately constrains the NH_3 yields.

Aiming to study the Ag component effect on the electrochemical properties, we decided to add Ag into FeCoNiCuGa to prepare FeCoNiCuGaAg and check its eNO_3RR and eNO_2RR LSVs, and CPE at −0.3 V (Figure 3a–c). Compared to FeCoNiCuGa, FeCoNiCuGaAg exhibits a positive NO_3RR onset potential near 0.25 V but lower current densities in the negative potential region (Figure 3a). However, the eNO_2RR LSVs of FeCoNiCuGa and FeCoNiCuGaAg exhibit a similar trend (Figure 3b), suggesting that these two materials have comparable apparent reaction kinetics toward eNO_2RR. To investigate the origin of the electrocatalytic performance of both electrocatalysts, the electrochemically active surface area (ECSA) measurements were conducted for FeCoNiCuGa and FeCoNiCuGaAg (Figure S11). The FeCoNiCuGaAg demonstrates higher double-layer capacitance (C_{dl}) than FeCoNiCuGa, indicating a higher ECSA. Despite this higher ECSA, FeCoNiCuGaAg shows a lower NH_3 FE than FeCoNiCuGa (Figure 3c), excluding surface area effects as the dominant factor. Meanwhile, the introduction of Ag shifts the NO_3RR onset potential positively and leads to a higher NO_2^- FE, suggesting weakened $*NO_2^-$ adsorption on FeCoNiCuGaAg, which consequently suppresses NH_3 formation. Therefore, the NH_3 selectivity is governed by intrinsic active-site properties, particularly the variations in $*NO_2^-$ binding strength, rather than morphology or specific surface area effects. Subsequently, the elemental occurrence frequencies of the bottom three electrocatalysts ranked by $j_{NO_2RR} - j_{HER}$ (also the bottom three Y_{NH_3} electrocatalysts) were analyzed, showing that both Zr and Mo appear most frequently (Figure S12, Table S1). Thus, FeCoNiCuGaZr, FeCoNiCuGaMo, and FeCoNiCuGaZrMo were synthesized and subsequently subjected to electrochemical measurements to analyze the degradation issue (Figure 3a–c). Mo addition causes a slight decline in both NO_3RR and NO_2RR LSVs of FeCoNiCuGaMo, while FeCoNiCuGaZr and FeCoNiCuGaZrMo exhibit inferior NO_3RR and NO_2RR performance (Figure 3a–c), demonstrating that Zr introduction leads to significant performance degradation (Figure 3a,b). Zr adding impedes eNO_2RR, thereby negatively affecting NH_3 yields (Figure 3c). Summarizing the study on elemental effects, the results from FeCoNiCuGaAg and FeCoNiCuGaZr electrochemical measurements with the previous observations on Ag-containing materials and the HMC descriptors, $*NO_2^-$ formation and its conversion to subsequent steps are critical in determining NH_3 production.

The analysis based on HMC descriptors and elemental roles of Ag and Zr identified $*NO_2^-/NO_2^-$ as the critical intermediates to NH_3 yields. Thus, elucidating $*NO_2^-$ behavior is essential for understanding the eNO_3RR mechanism within MEPT framework. Given that multi-component electrocatalysts could alter product distribution, the individual contributions of each component were investigated to better understand $*NO_2^-$ effect. Upon CPE, single-metal materials demonstrate significantly lower NH_3 FE and j_{NH_3} than FeCoNiCuGa (Figure 3e). NO_2^- is the dominant product on Cu and Ni whereas Co favors NH_3 formation, implying that Cu and Ni accelerate $*NO_2^-$ formation with a limited $*NO_2^-$ conversion effect while Co promotes $*NO_2^-$ reduction. Additionally, FeNiCuGaAg exhibits a diminished NO_2RR response and a higher NO_2^- FE than FeCoNiCuGaAg (Figures S13–S15), further confirming that the Co facilitates the eNO_2RR process to elevate NH_3 productivity. Meanwhile, Fe contributes to limited NH_3 FE; Ga exhibits the lowest j_{NH_3} (Figure 3e). A comparative analysis of FeCoNiCuGaAg and FeCoNiCuAg clarified that although FeCoNiCuAg has higher NO_3RR and NO_2RR responses than FeCoNiCuGaAg, the dominant product is NO_2^- (Figures S13–S15). As NO_3RR is a MEPT with 2-electron/proton transfer HER as a side reaction, the electrons/protons' behavior within HER could significantly affect eNO_3RR performance. FeCoNiCuAg demonstrates higher HER performance than FeCoNiCuGaAg (Figure S16), suggesting an intense proton transfer competition on FeCoNiCuAg during NH_3 formation. Ga has been identified as a promoter: introducing Ga makes NO_3RR intermediates protonation more preferential than HER. Thus, Ga assists in selective NH_3 formation. To further validate the $*NO_2^-$ effect, four-metal materials without Cu, Ni, or Ga (FeCoNiGa, FeCoCuGa, FeCoNiCu) were synthesized, followed by electrochemical measurements. All electrocatalysts exhibit lower eNO_3RR performance than FeCoNiCuGa, but similar NO_2RR trends (Figures 3d, S17). Upon CPEs, all electrocatalysts have comparable NH_3 FE but lower j_{NH_3} than that of FeCoNiCuGa (Figure 3e). The product current density is determined by the total current density and FE, which reflects the product formation rate [49]. CPE and eNO_3RR LSV results infer that the absence of Cu, Ni, or Ga hinders the NO_3RR to $*NO_2^-$ (Figure 3e). Therefore, despite all electrocatalysts maintaining comparable eNO_2RR activity to FeCoNiCuGa, inferior $*NO_2^-$ generation limits NH_3 production rate. The eNO_3RR Tafel analysis on FeCoNiCuGa toward NH_3 formation reveals a slope of 47 mV dec^{-1}, close to the theoretical value of 59 mV dec^{-1}, indicating that there is one electron transfer before rate-determining step (RDS) [50] and suggesting that NH_3 production is governed by $*NO_2^-$ formation (Figure 3f). The HMC descriptor shows that NH_3 productivity depends not only on NO_2^- conversion but also HER suppression, clarifying the importance of both eNO_2RR and HER to overall performance. The HER Tafel slope on FeCoNiCuGa is 145 mV dec^{-1} (Figure S18), indicating *H formation is the

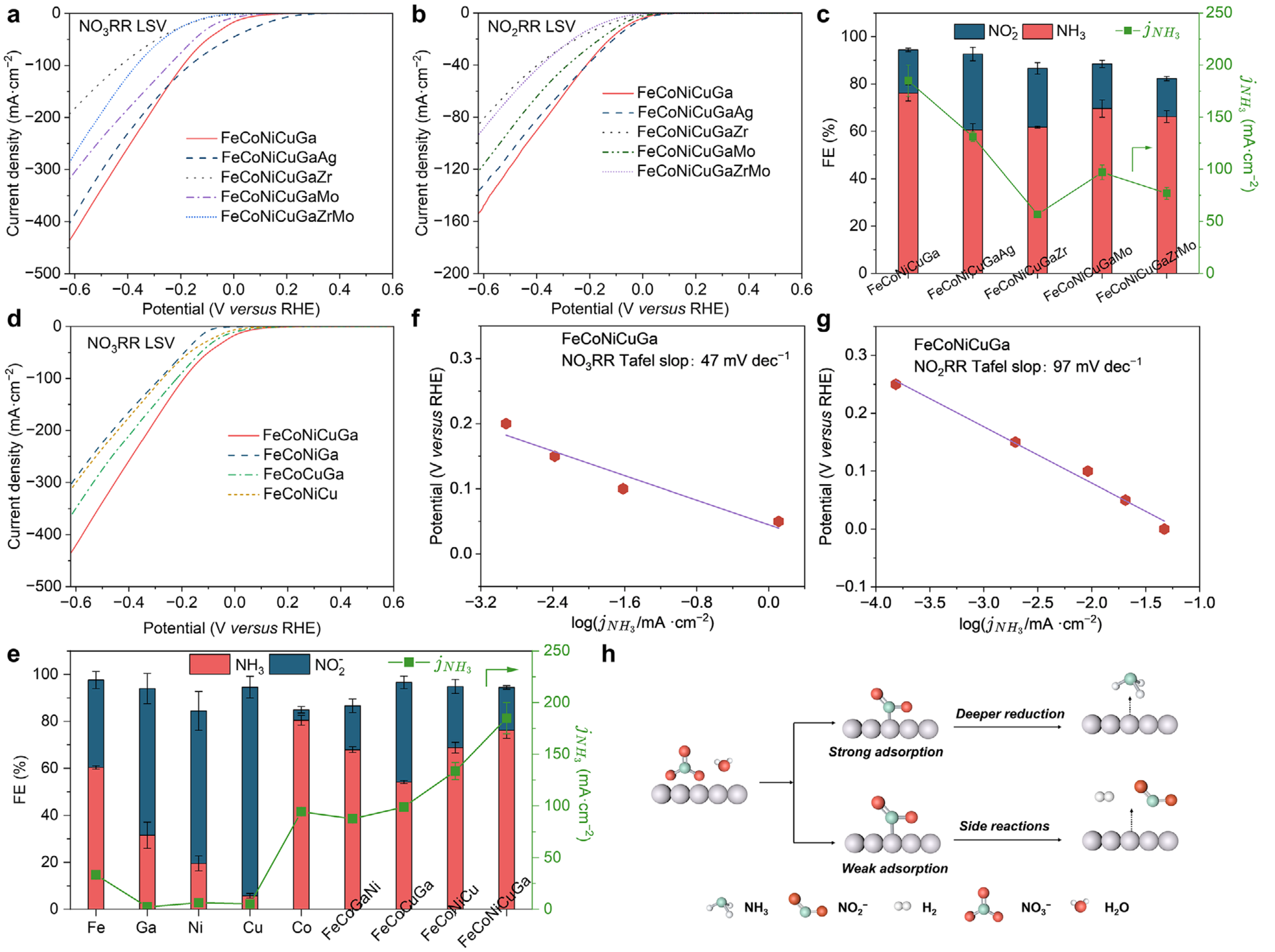

FIGURE 3 | (a) eNO$_3$RR, and (b) eNO$_2$RR LSVs of FeCoNiCuGa, FeCoNiCuGaAg, FeCoNiCuGaZr, FeCoNiCuGaMo, and FeCoNiCuGaZrMo in 0.1 M KOH + 1 M KNO$_3$ and 0.1 M KOH + 0.2 M KNO$_2$. (c) Products distribution and j_{NH_3} of FeCoNiCuGa, FeCoNiCuGaAg, FeCoNiCuGaZr, FeCoNiCuGaMo, and FeCoNiCuGaZrMo from NO$_3$RR CPE at −0.3 V in 0.1 M KOH + 1 M KNO$_3$. (d) NO$_3$RR LSVs of FeCoNiCuGa, FeCoNiCu, FeCoCuGa, and FeCoNiGa. (e) Products distribution and j_{NH_3} of Fe, Ga, Ni, Cu, Co, FeCoNiCuGa, FeCoNiCu, FeCoCuGa, and FeCoNiGa from NO$_3$RR CPE at −0.3 V in 0.1 M KOH + 1 M KNO$_3$. (f) eNO$_3$RR and (g) eNO$_2$RR Tafel slope for NH$_3$ formation on FeCoNiCuGa. (h) The schematic illustration of NO$_3$RR with different *NO$_2^-$ adsorption.

RDS [51, 52]. The FeCoNiCuGa shows an eNO$_2$RR Tafel slope of 97 mV dec^{-1} (Figure 3g), implying that eNO$_2$RR is restricted by NO$_2^-$ adsorption. *NO$_2^-$ competes with *H reducing *H coverage, inhibiting HER while promoting NH$_3$ formation. However, inadequate *NO$_2^-$ coverage causes low NH$_3$ productivity. Based on the Sabatier principle [53–55] and above results, we conclude that *NO$_2^-$ adsorption strength and its subsequent reduction dominate NH$_3$ productivity toward eNO$_3$RR (Figure 3h). Strong *NO$_2^-$ binding enables high *NO$_2^-$ coverage facilitating NH$_3$ formation while weak *NO$_2^-$ binding favors NO$_2^-$ formation.

To further support the role of *NO$_2^-$ in NH$_3$ formation, RRDE experiments were conducted on FeCoNiCuGa, FeCoNiCuGaAg, and FeCoNiCuGaZr. It is well known that the RRDE technique is a powerful electrochemical approach for studying kinetics, provided there is an effective mathematical model. In this study, we develop a new eNO$_3$RR kinetic model for the RRDE technique based on a previous ORR RRDE model (Figure 4a, details in Supporting Information). In our model, k_1 represents the direct 8-electron reduction of NO$_3^-$ to NH$_3$ without *NO$_2^-$ process; k_2 represents a 2-electron NO$_3^-$ reduction to *NO$_2^-$ process while k_{-2} represents the reversed path; k_3 is the deeper reduction of *NO$_2^-$ to NH$_3$; k_5 and k_6 represent *NO$_2^-$ desorption and NO$_2^-$ adsorption processes, respectively. Upon analyzing the $N\frac{I_D}{I_R}\omega^{-0.5}$ plots at different potentials, the tandem electrode and direct reduction processes can be distinguished. The Pt$_{0.5}$PdAu-coated Pt ring was used as the ring electrode and catalyzed an efficient NO$_2^-$ oxidation reaction (NO$_2$OR), even at 10 mM NO$_2^-$ concentration (Figure S19). Using the FeCoNiCuGa-coated Pt disk as the disk electrode, the collection efficiency (N) was calculated in 0.1 M KOH + 10 mM KNO$_3$ (Figure S20, Table S2). The average value (0.408) was adopted for subsequent calculations (Table S2). The RRDE setup was used to investigate the eNO$_3$RR and NO$_2$OR behaviors of FeCoNiCuGa at various rotation rates in 0.1 M KOH + 1 M KNO$_3$ (Figure 4b). During RRDE analysis, the ring potential was 1.675 V versus RHE, at which the oxygen evolution reaction (OER) current was relatively small (Figure S19). Within the potential range of 0.25–0.30 V

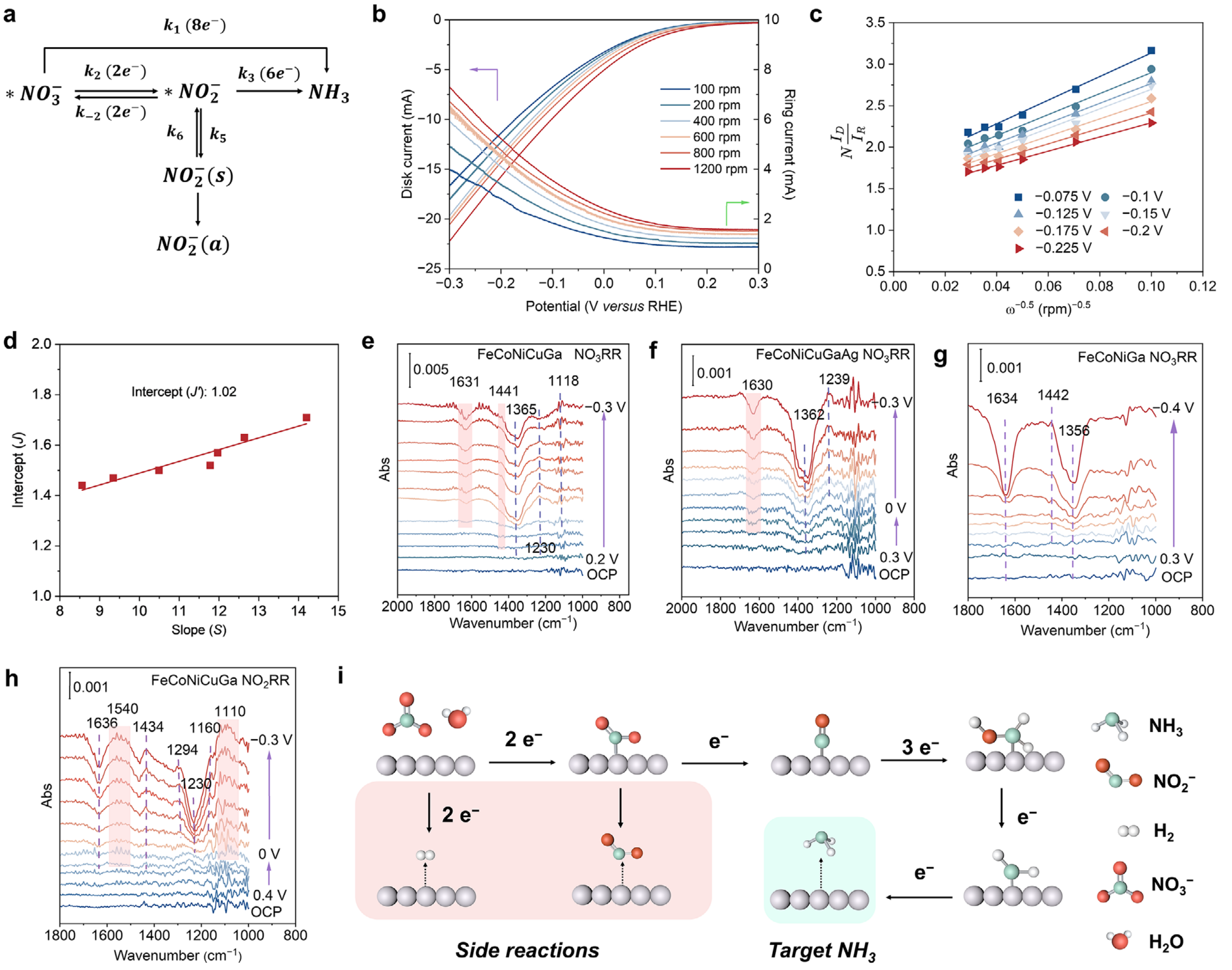

FIGURE 4 | (a) Schematic illustration of eNO$_3$RR RRDE model (* represents adsorption state; ***s*** represents surface; ***a*** represents bulk solution). (b) eNO$_3$RR LSVs and corresponding ring current of FeCoNiCuGa at different rotation rates in 0.1 M KOH + 1 M KNO$_3$. (c) Plots of $N\frac{I_D}{I_R}$–$\omega^{-0.5}$ for FeCoNiCuGa at −0.075 to −0.225 V versus RHE potential range. (d) The $J - S$ plots derived from the J and S values of $N\frac{I_D}{I_R}$–$\omega^{-0.5}$ plots at different potentials. In situ FT-IR spectra of NO$_3$RR on (e) FeCoNiCuGa, (f) FeCoNiCuGaAg, and (g) FeCoNiGa. (h) In situ FT-IR spectra of eNO$_2$RR on FeCoNiCuGa. (i) Schematic illustration of the proposed eNO$_3$RR reaction pathway.

versus RHE (Figure 4b), the NO$_3$RR had not yet been initiated on the disk electrode. The corresponding ring current exhibited a stable plateau, which mainly originated from the OER and could therefore be regarded as the background current. This background contribution was subtracted in the subsequent data analysis to obtain a more accurate net ring current associated with the oxidation of reaction intermediates (details in Supporting Information). Both NO$_3$RR and NO$_2$OR currents increase with rotation rates, indicating elevated mass transfer. The $N\frac{I_D}{I_R}$–$\omega^{-0.5}$ analysis was conducted from −0.075 to −0.225 V, where HER is negligible (Figure S21). From −0.075 to −0.225 V (with an interval of 0.025 V), the intercepts (J) obtained from $N\frac{I_D}{I_R}$–$\omega^{-0.5}$ plots at all potentials are greater than 1 (Figure 4c), suggesting the presence of the k_3 process ($J = 1 + 4\frac{k_3}{k_5}$, details in Supporting Information). Using J and the slopes (S) at different potentials to draw $J - S$ plots, the intercept (J') is 1.02 (Figure 4d), demonstrating that the k_1 process (direct NO$_3$RR to NH$_3$) is negligible on FeCoNiCuGa ($J' = 1 + 4\frac{k_1}{k_2}$, details in Supporting Information). Thus, the eNO$_3$RR on FeCoNiCuGa proceeds via consecutive processes of NO$_3$RR to *NO$_2^-$ and *NO$_2^-$ to NH$_3$. The RRDE analysis was also applied to FeCoNiCuGaZr, which exhibits lower J values than FeCoNiCuGa but follows the same consecutive pathway (Figures S22–S23). At a specific potential, the J value of the $N\frac{I_D}{I_R}$–$\omega^{-0.5}$ curve can be used to quantify the tendency of the k_3 to the k_5 process ($\frac{k_3}{k_5}$), signifying the importance of *NO$_2^-$ to final NH$_3$ productivity. The J values of FeCoNiCuGa, FeCoNiCuGaZr, and FeCoNiCuGaAg at −0.2 V were 1.48, 1.12, and 1.17, respectively (Figures 4c, S23, and S24). Compared to FeCoNiCuGaAg and FeCoNiCuGaZr, FeCoNiCuGa has a low *NO$_2^-$ desorption (k_5) rate and prefers k_3 process, which is advantageous for NH$_3$ formation. In contrast, in FeCoNiCuGaAg and FeCoNiCuGaZr, a suppressed k_3 process or an accelerated k_5 process results in limited NH$_3$ production. The RRDE analysis successfully excludes the existence of the direct eNO$_3$RR to NH$_3$

process and identifies the importance of $*NO_2^-$ conversion to NH_3 productivity in the tandem electrode process, providing a powerful reference for subsequent mechanism studies.

The overall pathway was determined using in situ Fourier transform infrared (FT-IR) spectra of eNO_3RR and eNO_2RR. Compared to the in situ FT-IR spectra of HER on FeCoNiCuGa (Figure S25), the downward peaks at 1365 cm^{-1} during NO_3RR correspond to NO_3^- consumption (Figure 4e) [56]. The depletion peaks at 1631 and ~3300 cm^{-1} indicate H_2O consumption, which is accompanied by considerable NO_3RR intermediates formation (Figures 4e, S26) [43, 57, 58]. The upward peaks at 1441 cm^{-1} represent the N—H vibration, indicating NH_3 formation [59, 60]. At 0.05 V, the $*NO_2^-$ bands at 1230 cm^{-1} appear [56, 61, 62] and attenuate from −0.1 V to −0.2 V. Correspondingly, new bands at 1118 cm^{-1} relating to N—O in $*NH_2OH$ emerge [61, 63–65], suggesting $*NO_2^-$ conversion. A downward peak corresponding to NO_3^- consumption emerges at 0.2 V on FeCoNiCuGaAg (Figure 4f), which is consistent with the NO_3RR LSV results. Additionally, H_2O depletion bands at 1630 cm^{-1} are observed on FeCoNiCuGaAg (Figure 4f) [43]. The $*NO_2^-$ peaks at 1239 cm^{-1} gradually strengthen from 0.1 to −0.3 V, suggesting sluggish $*NO_2^-$ conversion [56, 61, 62]. To further confirm the role of $*NO_2^-$, NO_3RR in situ FT-IR spectra were recorded on FeCoNiGa (Figure 4g). The absence of Cu hinders NO_3^- conversion to NO_2^-. Accordingly, the NO_3^- and H_2O consumption bands at 1356 [56] and 1635 cm$^{-[143]}$ and N—H vibration bands at 1442 cm^{-1} only appear at negative potentials [59, 60], demonstrating that inadequate $*NO_2^-$ formation restricts NH_3 yields.

The eNO_2RR in situ FT-IR spectra of FeCoNiCuGa, FeCoNiCuGaAg, and FeCoNiCuGaZr were used to explore the eNO_2RR to NH_3 pathway. In Figure 4h, the downward peaks at 1230 cm^{-1} on FeCoNiCuGa correspond to NO_2^- consumption, whereas the increased peaks around 1290 cm^{-1} are the characteristic peaks of $*NH_2$ [66]. The upward trends at 1540, 1434, 1160, and 1110 cm^{-1} indicate $*NO$ [67], NH_3 [59, 60], $*NH_2$ [60], and $*NH_2OH$ formation [61, 63–65], confirming the evolution of intermediates. Furthermore, the eNO_2RR in situ FT-IR spectra of FeCoNiCuGaAg are comparable to those of FeCoNiCuGa (Figure S27). In contrast, Zr impedes the eNO_2RR process, thus limiting $*NO_2^-$ transformation on FeCoNiCuGaZr. As a result, NO_2^- consumption can only be observed at negative potentials on FeCoNiCuGaZr (Figure S28). Additionally, the high Tafel slope of FeCoNiCuGaZr toward the NO_2RR (152 mV dec^{-1}, Figure S29) suggests that Zr weakens $*NO_2^-$ adsorption, thereby reducing surface coverage and negatively impacting NH_3 yield.

Correlating in situ FT-IR spectra with data analysis and the kinetic analyses based on RRDE unveils the significance of $*NO_2^-$ in NH_3 generation. A high $*NO_2^-$ formation rate and strong $*NO_2^-$ adsorption ensure sufficient $*NO_2^-$ coverage and subsequent transformation. In alkaline conditions, the electrode surface is typically negatively charged, which can result in electrostatic repulsion toward anions such as NO_3^-/NO_2^-. However, ion distributions within the electric double layer (EDL) cannot be described solely by classical electrostatic considerations alone [68]. During electrolysis, the high concentration K^+ cations could tune the local electric field near the electrode surface, which is benefit to the negatively charged species stabilization [69]. Furthermore, the continuous NO_3^-/NO_2^- consumption on the surface leads to a local concentration gradient, generating a diffusion flux toward the electrocatalyst surface. The combination of migration and diffusion enables the efficient transport of anions to the reaction plane in EDL. Moreover, the structural disorder of the amorphous matrix may result in a more heterogeneous local electric field distribution at the interface, potentially influencing the interfacial water structure. This interfacial modulation may contribute to the suppression of competing HER thus facilitating NO_3RR to NH_3. Based on these findings, we conclude that the overall NH_3 formation proceeds via the $NO_3^- \to * NO_2^- \to * NO \to * NH_2OH \to * NH_2 \to NH_3$ pathway (Figure 4i).

3 | Conclusion

In this study, based on the concept of direct simplification of MEPT, $j_{NO_2RR} - j_{HER}$ is strategically employed as a descriptor in BO-based HMC to accelerate eNO_3RR electrocatalysts screening. A highly efficient FeCoNiCuGa electrocatalyst with an NH_3 production rate of 9.8 mmol mg_{cat}^{-1} at −0.3 V is identified in just 1% of the trials across the entire candidate space. Our data analysis and mechanistic investigations including RRDE and in situ FT-IR spectra reveal that NH_3 productivity is governed by $*NO_2^-$ intermediates. Weak $*NO_2^-$ binding leads to low $*NO_2^-$ coverage, resulting in low NH_3 productivity. Conversely, strong $*NO_2^-$ binding enables high surface $*NO_2^-$ coverage, ensuring NH_3 productivity. Currently, AI platforms for MEPT reactions are restricted by the complex reaction process and limited data availability. This work provides a paradigm for identifying descriptors within complex reaction networks by incorporating key reaction steps into a human–machine collaborative workflow. Under alkaline conditions, HER kinetics are significantly suppressed, NO_2^- behaviors emerge as the dominant step that governs the overall reaction rate, which provides an experimentally accessible basis for constructing the descriptor. Despite the pronounced changes in the interfacial local environments, electron donors, and electric double layer structures under neutral or acidic conditions, the same dimensional reduced principle can still guide the design of new descriptors. This work successfully decouples the NO_3RR process and integrating AI platforms into the MEPT framework and clearly elucidates the crucial intermediates evolution at the solid–liquid interface, establishing a mechanistic foundation for future electrocatalytic applications.

Author Contributions

Yingying Cheng: methodology, data curation, investigation, validation, formal analysis, visualization, writing – original draft, writing – review and editing. **Masaki Takeguchi:** methodology, data curation, investigation, validation, formal analysis, visualization. **Abraham Castro Garcia:** methodology, data curation, investigation, validation, formal analysis, visualization, writing – review and editing. **Ken Sakaushi:** conceptualization, methodology, data curation, investigation, validation, formal analysis, supervision, funding acquisition, visualization, project administration, resources, writing – review and editing, writing – original draft.

Acknowledgements

This work was supported by the MEXT Program: Data Creation and Utilization-Type Material Research and Development Project Grant Number JPMXP1122712807, and Japan Science and Technology Agency (JST) as part of Adopting Sustainable Partnerships for Innovative Research Ecosystem (ASPIRE), Grant Number JPMJAP2421. The authors are indebted to the National Institute for Material Science.

Conflicts of Interest

The authors declare no conflicts of interest.

Data Availability Statement

The data that support the findings of this study are available on request from the corresponding author. The data are not publicly available due to privacy or ethical restrictions.

References

1. R. Gurney, "The Quantum Mechanics of Electrolysis," *Proceedings of The Royal Society of London Series A* 134 (1931): 137–154.

2. R. Dogonadze, A. Kuznetsov, and V. Levich, "Quantum Theory of Hydrogen Overvoltage," *Elektrokhim* 3 (1967): 739–742.

3. W. Schmickler, "The Influence of the Inner Solvation Sphere on Electrochemical Outer Sphere Redox Reactions of Transition Metal Ions—A Quantum Mechanical Approach," *Berichte der Bunsengesellschaft für physikalische Chemie* 77 (1973): 991–994, https://doi.org/10.1002/bbpc.19730771048.

4. A. Soudackov and S. Hammes-Schiffer, "Multistate Continuum Theory for Multiple Charge Transfer Reactions in Solution," *Journal of Chemical Physics* 111 (1999): 4672–4687, https://doi.org/10.1063/1.479229.

5. M. T. M. Koper, "Thermodynamic Theory of Multi-electron Transfer Reactions: Implications for Electrocatalysis," *Journal of Electroanalytical Chemistry* 660 (2011): 254–260, https://doi.org/10.1016/j.jelechem.2010.10.004.

6. K. Sakaushi, T. Kumeda, S. Hammes-Schiffer, M. M. Melander, and O. Sugino, "Advances and Challenges for Experiment and Theory for Multi-electron Multi-proton Transfer at Electrified Solid–liquid Interfaces," *Physical Chemistry Chemical Physics* 22 (2020): 19401–19442, https://doi.org/10.1039/D0CP02741C.

7. R. R. Adžić, S. Strbac, and N. Anastasijević, "Electrocatalysis of Oxygen on Single Crystal Gold Electrodes," *Materials Chemistry and Physics* 22 (1989): 349–375.

8. H. Kita, S. Ye, and Y. Gao, "Mass Transfer Effect in Hydrogen Evolution Reaction on Pt Single-Crystal Electrodes in Acid Solution," *Journal of Electroanalytical Chemistry* 334 (1992): 351–357, https://doi.org/10.1016/0022-0728(92)80583-P.

9. N. M. Marković, R. R. Adžić, B. Cahan, and E. Yeager, "Structural Effects in Electrocatalysis: Oxygen Reduction on Platinum Low Index Single-Crystal Surfaces in Perchloric Acid Solutions," *Journal of Electroanalytical Chemistry* 377 (1994): 249–259, https://doi.org/10.1016/0022-0728(94)03467-2.

10. R. Jinnouchi and A. B. Anderson, "Electronic Structure Calculations of Liquid-solid Interfaces: Combination of Density Functional Theory and Modified Poisson-Boltzmann Theory," *Physical Review B* 77 (2008): 245417, https://doi.org/10.1103/PhysRevB.77.245417.

11. K. Ojha, N. Arulmozhi, D. Aranzales, and M. T. M. Koper, "Double Layer at the Pt(111)–Aqueous Electrolyte Interface: Potential of Zero Charge and Anomalous Gouy–Chapman Screening," *Angewandte Chemie International Edition* 59 (2020): 711–715, https://doi.org/10.1002/anie.201911929.

12. T. Kumeda, L. Laverdure, K. Honkala, M. M. Melander, and K. Sakaushi, "Cations Determine the Mechanism and Selectivity of Alkaline Oxygen Reduction Reaction on Pt(111)," *Angewandte Chemie International Edition* 62 (2023): e202312841.

13. Y. Yang, R. G. Agarwal, P. Hutchison, et al., "Inverse Kinetic Isotope Effects in the Oxygen Reduction Reaction at Platinum Single Crystals," *Nature Chemistry* 15 (2023): 271–277.

14. F. Jiao and B. Xu, "Electrochemical Ammonia Synthesis and Ammonia Fuel Cells," *Advanced Materials* 31 (2019): e1805173, https://doi.org/10.1002/adma.201805173.

15. B. H. Ko, B. Hasa, H. Shin, Y. Zhao, and F. Jiao, "Electrochemical Reduction of Gaseous Nitrogen Oxides on Transition Metals at Ambient Conditions," *Journal of the American Chemical Society* 144 (2022): 1258–1266, https://doi.org/10.1021/jacs.1c10535.

16. International Renewable Energy Agency, Ammonia Energy Association. IRENA Innovation Outlook Renewable Ammonia. can be found under: https://www.irena.org/publications/2022/May/Innovation-Outlook-Renewable-Ammonia, 2022 (accessed: 19 September 2024).

17. S. Han, H. Li, T. Li, et al., "Ultralow Overpotential Nitrate Reduction to Ammonia via a Three-step Relay Mechanism," *Nature Catalysis* 6 (2023): 402–414, https://doi.org/10.1038/s41929-023-00951-2.

18. K. Dong, Y. Yao, H. Li, et al., "H_2O_2-Mediated Electrosynthesis of Nitrate From Air," *Nature Synthesis* 3 (2024): 763–773, https://doi.org/10.1038/s44160-024-00522-8.

19. C. Chen, X. Zhu, X. Wen, et al., "Coupling N_2 and CO_2 in H_2O to Synthesize Urea Under Ambient Conditions," *Nature Chemistry* 12 (2020): 717–724, https://doi.org/10.1038/s41557-020-0481-9.

20. P. Li, R. Li, Y. Liu, M. Xie, Z. Jin, and G. Yu, "Pulsed Nitrate-to-Ammonia Electroreduction Facilitated by Tandem Catalysis of Nitrite Intermediates," *Journal of the American Chemical Society* 145 (2023): 6471–6479, https://doi.org/10.1021/jacs.3c00334.

21. S. Zhu, K. Liu, Z. Feng, H. Jiang, and J. Lin, "The Dual Active Site Ni_3Sn_2-$NiSnO_x$ Alloy-Oxide Catalysts via Sn-Modulated Ni Coordination for Efficient Ammonia Synthesis," *Nano Research Energy* 4 (2025): e9120188, https://doi.org/10.26599/NRE.2025.9120188.

22. H. Zhang, H. Wang, X. Cao, et al., "Unveiling Cutting-Edge Developments in Electrocatalytic Nitrate-to-Ammonia Conversion," *Advanced Materials* 36 (2024): e2312746, https://doi.org/10.1002/adma.202312746.

23. J. Liang, Z. Li, L. Zhang, et al., "Advances in Ammonia Electrosynthesis From Ambient Nitrate/Nitrite Reduction," *Chemistry* 9 (2023): 1768–1827, https://doi.org/10.1016/j.chempr.2023.05.037.

24. X. Fan, C. Liu, X. He, et al., "Efficient Electrochemical Co-Reduction of Carbon Dioxide and Nitrate to Urea With High Faradaic Efficiency on Cobalt-Based Dual-Sites," *Advanced Materials* 36 (2024): e2401221, https://doi.org/10.1002/adma.202401221.

25. Z. Y. Wu, M. Karamad, X. Yong, et al., "Electrochemical Ammonia Synthesis via Nitrate Reduction on Fe Single Atom Catalyst," *Nature Communications* 12 (2021): 2870, https://doi.org/10.1038/s41467-021-23115-x.

26. K. B. Prater and A. J. Bard, "Rotating Ring-Disk Electrodes III. Catalytic and ECE Reactions," *Journal of the Electrochemical Society* 117 (1970): 1517–1520, https://doi.org/10.1149/1.2407362.

27. A. Damjanovic, M. A. Genshaw, and J. O. M. Bockris, "Distinction Between Intermediates Produced in Main and Side Electrodic Reactions," *Journal of Chemical Physics* 45 (1966): 4057–4059, https://doi.org/10.1063/1.1727457.

28. H. S. Wroblowa, P. Yen Chi, and G. Razumney, "Electroreduction of Oxygen a New Mechanistic Criterion," *Journal of Electroanalytical Chemistry and Interfacial Electrochemistry* 69 (1976): 195–201, https://doi.org/10.1016/S0022-0728(76)80250-1.

29. A. J. Appleby and M. Savy, "Kinetics of Oxygen Reduction Reactions Involving Catalytic Decomposition of Hydrogen Peroxide," *Journal of Electroanalytical Chemistry and Interfacial Electrochemistry* 92 (1978): 15–30, https://doi.org/10.1016/S0022-0728(78)80113-2.

30. R. W. Zurilla, R. K. Sen, and E. Yeager, "The Kinetics of the Oxygen Reduction Reaction on Gold in Alkaline Solution," *Journal of the Electrochemical Society* 125 (1978): 1103–1109, https://doi.org/10.1149/1.2131628.

31. J. C. Huang, R. K. Sen, and E. Yeager, "Oxygen Reduction on Platinum in 85% Orthophosphoric Acid," *Journal of the Electrochemical Society* 126 (1979): 786–792, https://doi.org/10.1149/1.2129139.

32. X. Xing, D. A. Scherson, and C. Mak, "The Electrocatalytic Reduction of Nitrate Mediated by Underpotential-Deposited Cadmium on Gold and Silver Electrodes in Acid Media," *Journal of the Electrochemical Society* 137 (1990): 2166–2175, https://doi.org/10.1149/1.2086905.

33. N. M. Marković, H. A. Gasteiger, and P. N. Ross, "Oxygen Reduction on Platinum Low-Index Single-Crystal Surfaces in Alkaline Solution: Rotating Ring DiskPt(hkl) Studies," *Journal of Physical Chemistry* 100 (1996): 6715–6721, https://doi.org/10.1021/jp9533382.

34. U. A. Paulus, T. J. Schmidt, H. A. Gasteiger, and R. J. Behm, "Oxygen Reduction on a High-Surface Area Pt/Vulcan Carbon Catalyst: A Thin-Film Rotating Ring-Disk Electrode Study," *Journal of Electroanalytical Chemistry* 495 (2001): 134–145, https://doi.org/10.1016/S0022-0728(00)00407-1.

35. Y. Chen, H. Zhu, M. Rasmussen, and D. Scherson, "Rational Design of Electrocatalytic Interfaces: The Multielectron Reduction of Nitrate in Aqueous Electrolytes," *Journal of Physical Chemistry Letters* 1 (2010): 1907–1911, https://doi.org/10.1021/jz1005253.

36. Z. W. Chen, J. Li, P. Ou, et al., "Unusual Sabatier Principle on High Entropy Alloy Catalysts for Hydrogen Evolution Reactions," *Nature Communications* 15 (2024): 359, https://doi.org/10.1038/s41467-023-44261-4.

37. D. Yin, B. Li, B. Gao, et al., "Overcoming Energy-Scaling Barriers: Efficient Ammonia Electrosynthesis on High-Entropy Alloy Catalysts," *Advanced Materials* 37 (2025): e2415739.

38. K. Sakaushi, W. Hoisang, and R. Tamura, "Human–Machine Collaboration for Accelerated Discovery of Promising Oxygen Evolution Electrocatalysts With on-Demand Elements," *ACS Central Science* 9 (2023): 2216–2224, https://doi.org/10.1021/acscentsci.3c01009.

39. S. Nie, Y. Xiang, L. Wu, et al., "Active Learning Guided Discovery of High Entropy Oxides Featuring High H_2-production," *Journal of the American Chemical Society* 146 (2024): 29325–29334, https://doi.org/10.1021/jacs.4c06272.

40. H. Xu, Y. Ma, J. Chen, W. X. Zhang, and J. Yang, "Electrocatalytic Reduction of Nitrate—A Step towards a Sustainable Nitrogen Cycle," *Chemical Society Reviews* 51 (2022): 2710–2758, https://doi.org/10.1039/D1CS00857A.

41. K. Fan, W. Xie, J. Li, et al., "Active Hydrogen Boosts Electrochemical Nitrate Reduction to Ammonia," *Nature Communications* 13 (2022): 7958, https://doi.org/10.1038/s41467-022-35664-w.

42. E. Murphy, Y. Liu, I. Matanovic, et al., "Elucidating Electrochemical Nitrate and Nitrite Reduction Over Atomically-dispersed Transition Metal Sites," *Nature Communications* 14 (2023): 4554, https://doi.org/10.1038/s41467-023-40174-4.

43. S. Liang, X. Teng, H. Xu, L. Chen, and J. Shi, "H* Species Regulation by Mn-Co$(OH)_2$ for Efficient Nitrate Electro-Reduction in Neutral Solution," *Angewandte Chemie International Edition* 63 (2024): e202400206.

44. A. Bagger, W. Ju, A. S. Varela, P. Strasser, and J. Rossmeisl, "Electrochemical CO_2 Reduction: A Classification Problem," *Chemphyschem* 18 (2017): 3266–3273, https://doi.org/10.1002/cphc.201700736.

45. X. Ouyang, W. Qiao, Y. Yang, et al., "Intensifying Interfacial Reverse Hydrogen Spillover for Boosted Electrocatalytic Nitrate Reduction to Ammonia," *Angewandte Chemie International Edition* 64 (2025): e202422585.

46. Q. Yang, W. Xu, S. Gong, et al., "Atomically Dispersed Lewis Acid Sites Boost 2-electron Oxygen Reduction Activity of Carbon-based Catalysts," *Nature Communications* 11 (2020): 5478, https://doi.org/10.1038/s41467-020-19309-4.

47. K.-H. Kim, H. Lee, X. Huang, et al., "Energy-Efficient Electrochemical Ammonia Production From Dilute Nitrate Solution," *Energy & Environmental Science* 16 (2023): 663–672, https://doi.org/10.1039/D2EE03461A.

48. J. Yu, R. T. Gao, X. Guo, N. Truong Nguyen, L. Wu, and L. Wang, "Electrochemical Nitrate Reduction to Ammonia on AuCu Single-Atom Alloy Aerogels Under Wide Potential Window," *Angewandte Chemie International Edition* 64 (2024): e202415975.

49. Y. Liu and C. C. L. McCrory, "Modulating the Mechanism of Electrocatalytic CO_2 Reduction by Cobalt Phthalocyanine Through Polymer Coordination and Encapsulation," *Nature Communications* 10 (2019): 1683, https://doi.org/10.1038/s41467-019-09626-8.

50. K. Sakaushi, "Quantum Electrocatalysts: Theoretical Picture, Electrochemical Kinetic Isotope Effect Analysis, and Conjecture to Understand Microscopic Mechanisms," *Physical Chemistry Chemical Physics* 22 (2020): 11219–11243, https://doi.org/10.1039/D0CP01052A.

51. M. T. M. Koper, "Analysis of Electrocatalytic Reaction Schemes: Distinction Between Rate-determining and Potential-Determining Steps," *Journal of Solid State Electrochemistry* 17 (2012): 339–344, https://doi.org/10.1007/s10008-012-1918-x.

52. H. Prats and K. Chan, "The Determination of the HOR/HER Reaction Mechanism From Experimental Kinetic Data," *Physical Chemistry Chemical Physics* 23 (2021): 27150–27158, https://doi.org/10.1039/D1CP04134G.

53. J. K. Nørskov, T. Bligaard, A. Logadottir, et al., "Trends in the Exchange Current for Hydrogen Evolution," *Journal of the Electrochemical Society* 152 (2005): J23–J26.

54. J. Greeley, T. F. Jaramillo, J. Bonde, I. Chorkendorff, and J. K. Nørskov, "Computational High-throughput Screening of Electrocatalytic Materials for Hydrogen Evolution," *Nature Materials* 5 (2006): 909–913, https://doi.org/10.1038/nmat1752.

55. Z. W. Seh, J. Kibsgaard, C. F. Dickens, I. Chorkendorff, J. K. Nørskov, and T. F. Jaramillo, "Combining Theory and Experiment in Electrocatalysis: Insights Into Materials Design," *Science* 355 (2017): eaad4998, https://doi.org/10.1126/science.aad4998.

56. E. Pérez-Gallent, M. C. Figueiredo, I. Katsounaros, and M. T. M. Koper, "Electrocatalytic Reduction of Nitrate on Copper Single Crystals in Acidic and Alkaline Solutions," *Electrochimica Acta* 227 (2017): 77–84, https://doi.org/10.1016/j.electacta.2016.12.147.

57. S. Liu, T. Qian, M. Wang, et al., "Proton-Filtering Covalent Organic Frameworks With Superior Nitrogen Penetration Flux Promote Ambient Ammonia Synthesis," *Nature Catalysis* 4 (2021): 322–331, https://doi.org/10.1038/s41929-021-00599-w.

58. Y. Wan, M. Pei, Y. Tang, et al., "Interfacial Water Regulation for Nitrate Electroreduction to Ammonia at Ultralow Overpotentials," *Advanced Materials* 37 (2025): e2417696, https://doi.org/10.1002/adma.202417696.

59. Y. Zhang, H. Zheng, K. Zhou, et al., "Conjugated Coordination Polymer as a New Platform for Efficient and Selective Electroreduction of Nitrate Into Ammonia," *Advanced Materials* 35 (2023): e2209855.

60. S. Lu, G. Lin, H. Yan, et al., "In Situ Facet Transformation Engineering over Co_3O_4 for Highly Efficient Electroreduction of Nitrate to Ammonia," *ACS Catalysis* 14 (2024): 14887–14894.

61. J. Y. Fang, Q. Z. Zheng, Y. Y. Lou, et al., "Ampere-Level Current Density Ammonia Electrochemical Synthesis Using CuCo Nanosheets Simulating Nitrite Reductase Bifunctional Nature," *Nature Communications* 13 (2022): 7899, https://doi.org/10.1038/s41467-022-35533-6.

62. X. Huang, Y. Li, S. Xie, et al., "The Tandem Nitrate and CO_2 Reduction for Urea Electrosynthesis: Role of Surface N-Intermediates in CO_2 Capture and Activation," *Angewandte Chemie International Edition* 63 (2024): e202403980, https://doi.org/10.1002/anie.202403980.

63. Y. Zhou, W. Zhang, P. Guo, et al., "Continuous Regulation of Cu Electronic States by Rectifying Schottky Contacts Enhancing Electrochemical Nitrate Reduction to Ammonia," *Inorganic Chemistry Frontiers* 11 (2024): 3503–3510, https://doi.org/10.1039/D4QI00614C.

64. Y. Tang, Z. Jiang, Y. Yuan, et al., "Selective Electrosynthesis of Hydroxylamine From Aqueous Nitrate/Nitrite by Suppressing Further Reduction," *Nature Communications* 15 (2024): 9800, https://doi.org/10.1038/s41467-024-54204-2.

65. Y. Liu, Z. Zhuang, Y. Liu, et al., “Shear-Strained Pd Single-Atom Electrocatalysts for Nitrate Reduction to Ammonia,” *Angewandte Chemie International Edition* 63 (2024): e202411396.

66. K. Yang, S. H. Han, C. Cheng, C. Guo, T. Li, and Y. Yu, “Unveiling the Reaction Mechanism of Nitrate Reduction to Ammonia over Cobalt-Based Electrocatalysts,” *Journal of the American Chemical Society* 146 (2024): 12976–12983, https://doi.org/10.1021/jacs.3c13517.

67. W. Liao, J. Wang, G. Ni, et al., “Sustainable Conversion of Alkaline Nitrate to Ammonia at Activities Greater than 2 A cm^{-2},” *Nature Communications* 15 (2024): 1264, https://doi.org/10.1038/s41467-024-45534-2.

68. P. Li, Y. Jiao, J. Huang, and S. Chen, “Electric Double Layer Effects in Electrocatalysis: Insights From Ab Initio Simulation and Hierarchical Continuum Modeling,” *JACS Au* 3 (2023): 2640–2659, https://doi.org/10.1021/jacsau.3c00410.

69. W. Wen, S. Fang, Y. Zhou, Y. Zhao, P. Li, and X. Y. Yu, “Modulating the Electrolyte Microenvironment in Electrical Double Layer for Boosting Electrocatalytic Nitrate Reduction to Ammonia,” *Angewandte Chemie International Edition* 63 (2024): e202408382, https://doi.org/10.1002/anie.202408382.

Supporting Information

Additional supporting information can be found online in the Supporting Information section.

Supporting File: anie72478-sup-0001-SuppMat.docx.